Efficient Parahydrogen Induced ^{13}C Hyperpolarization on a Microfluidic Device

Sylwia J. Barker,[†,‡] Laurynas Dagys,[†,¶] Malcolm H. Levitt,[†] and Marcel Utz[*,†,‡]

†*School of Chemistry, University of Southampton, United Kingdom*

‡*Institute of Microstructure Technology, Karlsruhe Institute of Technology, Germany*

¶*Institute of Chemical Physics, Vilnius University, Lithuania*

E-mail: marcel.utz@kit.edu

Abstract

In this work we demonstrate the direct production and detection of ^{13}C-hyperpolarized fumarate by parahydrogen-induced polarization (PHIP) in a microfluidic Lab-on-a-Chip (LoC) device and achieve 8.5% ^{13}C polarization. This is the first demonstration of ^{13}C-hyperpolarization of a metabolite by PHIP in a microfluidic device. LoC technology allows the culture of mammalian cells in a highly controlled environment, providing an important tool for the life sciences. In-situ preparation of hyperpolarized metabolites greatly enhances the ability to quantify metabolic processes in such systems by microfluidic NMR. PHIP of ^{1}H nuclei has been successfully implemented in microfluidic systems, with mass sensitivities in the range of pmol$\sqrt{\text{s}}$, but only with low yields. Metabolic NMR requires high-yield production of hyperpolarized metabolites with longer spin life times than is possible with ^{1}H. This can be achieved by transfer of the polarization onto ^{13}C nuclei, which exhibit much longer T_1 relaxation times.

We report an improved microfluidic PHIP device that has been optimised using a finite element model that achieves a more than 20-fold improvement in the yield of the hyperpolarized

product. It is shown that this enables detailed kinetic studies of the hydrogenation of propargyl acetate to allyl acetate, as well as the direct production of ^{13}C hyperpolarized fumarate.

Introduction

Microfluidic Lab-on-a-Chip (LoC) technology finds applications across many disciplines but perhaps one of the most important is its use in the culture of biological systems. Especially in the context of oncology research, Organ-on-a-Chip (OoC) technology that can culture cells, cell aggregates, or tissues, is increasingly adopted in drug development.[1–3] Since the technology can use human cells, it is potentially more accurate than animal models. Moreover, the need to reduce animal testing in research is widely recognized. Apart from simply substituting Petri dishes and flasks used in conventional cultures with more compact and cost-effective alternatives, microfluidic technology enables precise control over the environment in a repeatable manner. This is a vital advantage in biological research, where manipulation of the local or systemic environment is necessary to study cellular processes and functions as well as their response to external stimuli such as drugs,[4] therapeutic targets,[5–7] toxins,[8,9] oxygen or nutrient supply.[10,11] However, sensitive, non-invasive and real-time *operando* characterization is challenging in these systems due to inherently small sizes of these devices. Here we demonstrate a LoC device capable of formation and detection of ^{13}C-hyperpolarized metabolites at the microscale.

Hyperpolarization is a promising tool for oncology research as it enables the enhancement of metabolite signals in a Nuclear Magnetic Resonance (NMR) spectrum or image (MRI) by several orders of magnitude. This allows provision of real-time and quantitative information on the kinetics of downstream metabolites in healthy and diseased systems. The method has been used *in vivo* for metabolic profiling of tumours such glioma,[12,13] hepatocellular carcinoma, lymphoma,[14,15] pancreatic[16] and breast cancers.[17,18] More generally, high-resolution NMR spectroscopy is an ideal technique to follow chemical reactions and monitor biological systems in LoC and OoC due to its non-invasive nature, chemical specificity and the ability to quantify metabolites. However, the

integration of microfluidic systems with NMR spectroscopy is technically challenging.[19] Significant progress in this area over the past few years has led to the development of microfluidic culture systems with integrated NMR metabolomics observation,[20–22] as well as NMR-based microfluidic reaction monitoring systems.[23] Due to the small volumes involved (μL to pL), sensitivity is a strong limiting factor for microfluidic NMR. Hyperpolarization, by offering several orders of magnitude in signal enhancements, can potentially address this. However, nuclear spin relaxation limits the lifetime of hyperpolarized species. This makes it crucial to produce them in immediate proximity of their usage. This motivates our efforts to directly integrate the production of hyperpolarized materials into microfluidic systems.

Parahydrogen-Induced Polarization (PHIP) makes it possible to enhance NMR signals by up to 5 orders of magnitude.[24,25] PHIP utilises *para*-hydrogen ($p-H_2$), the singlet nuclear spin isomer of molecular hydrogen, as a source of spin order. The nuclear spin order is transferred to a target molecule via a chemical reaction of $p-H_2$ with an unsaturated molecule in the presence of an organometallic catalyst. The chemical reaction is followed by spin manipulations to transfer the parahydrogen-derived spin order to a desired nucleus, and may include purification steps to remove unwanted compounds.[26]

LoC devices can be used to implement some or all of these processes, thus offering the possibility of integrating the production, purification, and application of hyperpolarized species to a biological system at the microscale. Mass sensitives of the order of pmol/s for ^{1}H were reported using such systems.[27] Nonetheless, the yield obtained in this reaction falls short of the requirements for biological applications, particularly since further transformations such as purification and cleavage are required to effectively utilise the hyperpolarized material. To understand the interplay of the chemical, spatial and spin dynamics occurring on the microfluidic device proposed by Eills *et al.* Ostrowska *et al.*[28] developed a finite element model of reaction and found that insufficient uptake of hydrogen was the limiting factor of the reaction.

In the present contribution, we utilise the finite element model to build a microfluidic device that maximises hydrogen uptake. Additionally, we introduce a variable temperature control to

regulate the temperature at the sample detection chamber and use this to study the kinetics of propargyl acetate hydrogenation. We tailor these results to produce fumarate and report for the first time the formation, production and detection of ^{13}C-hyperpolarized metabolite by PHIP in a LoC device.

Background

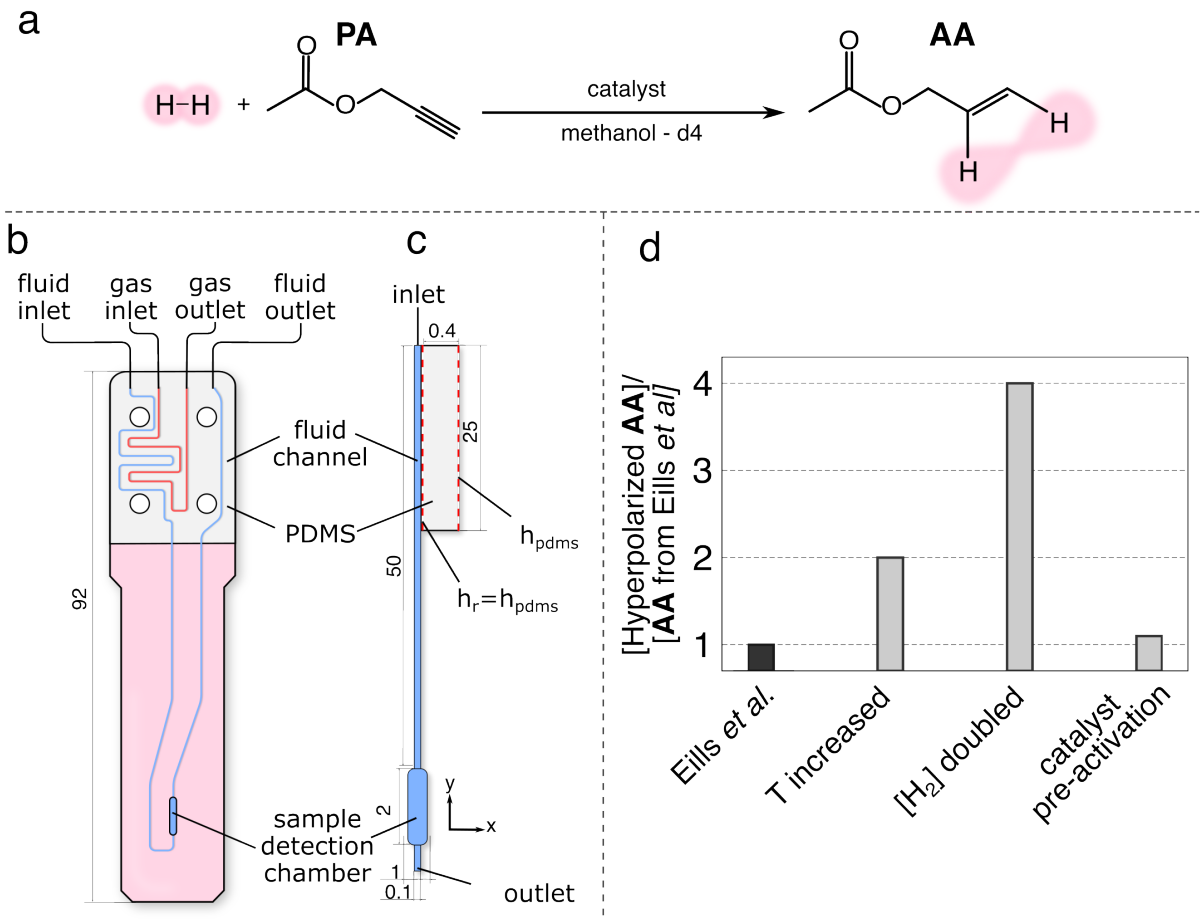

Figure 1: a) Propargyl acetate hydrogenation reaction scheme. b) Top view of the microfluidic device ($\alpha-$chip) used by Eills *et al.*[27] c) Finite element simulation domain of the $\alpha-$chip reported by Ostrowska *et al.*[28] d) Increase in concentration of hyperpolarized **AL** obtained from Eills *et al.*[27] and three independent scenarios predicted by the model developed in Ref.[28]

Alkyne esters represent an important class of targets as they offer the possibly to hyperpolarize a range of carboxylate containing molecules such as pyruvate or lactate via the side-arm

hydrogenation (PHIP-SAH) strategy.[29–32] Here we study the production of hyperpolarized allyl acetate (**AL**) as shown in Fig. 1a. This chemical transformation entails the utilization of parahydrogen gas and a rhodium catalyst to catalyze the hydrogenation of propargyl acetate (**PR**). Fig. 1b shows the top view of the microfluidic device (the $\alpha-$chip) reported by Eills *et al.*[27] used to perform this reaction at the microscale. The precursor solution that included propargyl acetate and the organometallic catalyst was delivered into the fluid channel shown in blue using a syringe pump, and parahydrogen gas was delivered into the chip via a separate gas channel (red). A semi-permeable polydimethylsiloxane (PDMS) membrane enabled gas diffusion into the chip thus the chemical reaction took place directly on the chip. The products were detected at the sample detection chamber. To simulate the reaction occurring on the chip, Ostrowska *et al.*[28] simplified the chip geometry to a 2D representation that contained: an inlet, an outlet, the fluid channel, PDMS membrane, and the sample detection chamber as depicted in Fig. 1c. Simualtion details are included in the SI.

The black bar in Fig. 1d represents the concentration of **AL** obtained from Eills *et al.*,[27] while the grey bars correspond to three scenarios predicted by the model developed by Ostrowska *et al.*. In the first scenario the temperature was increased by 10°C, in the second case the concentration of hydrogen was doubled, and lastly the catalyst activation rate was increased 10 times. The corresponding yield of **AL** was 0.6 mM, 1.2 mM, and 0.45 mM. Since the only significant concentration increase was observed by increasing the concentration of hydrogen, it was concluded that in order to increase the yield of **AL**, the first step must be an improvement of the hydrogen uptake.

Materials and Methods

Microfluidic Set Up

The microfluidic device, also referred to as the chip, was manufactured from polycarbonate (PC) (Self Adhesive Supplies, UK) following the protocol outlined in Ref.[33] Briefly, devices were cut out with a LS3040 CO_2 laser cutter (HPC Laser, United Kingdom) from three layers of polycar-

bonate sheet material with 0.25, 0.5, and 0.25 mm thickness for the top, middle, and bottom layers, respectively. The sample chamber and channels were cut through the top layer and engraved in the middle and bottom layers. After plasma activating using Corona Treater (Electro-Technic Products, USA), each layer was coated with 18 μL of plasticiser (5 v/v% dibuthyl phtalate in isopropyl alcohol). Then the layers were dried for 15 mins at 65°C, assembled and bonded together under pressure and heat (5 tonnes, 85°C).

The microfluidic assembly consisted of the chip interposed between two 1 mm PDMS membranes (Shielding Solutions, UK) held together by the fluidic interface (ProtoLabs, UK). Connectors for 1/16" fluid and gas lines (Cole Parmer, UK) facilitated the delivery of substrates onto the chip shown in Fig 2. PDMS membranes that covered the upper part of the chip served a dual purpose. Firstly they promoted diffusion of hydrogen into the liquid channel and secondly, they enabled sealing of the assembly.

All experiments were conducted on a Bruker AVANCE III spectrometer operating at 11.7 T magnetic field. The microfluidic assembly was placed inside of a stripline-based micro-NMR probe for detection[34] as shown in Fig 2. The probe was equipped with hydrothermal sleeves that housed a thermistor regulated by temperature controller, allowing efficient heating of the sample detection chamber only. The calibration of the heater was recorded by Rogers *et al.* and shows the temperature variation of $\pm$ 3°C, which is sufficient for this application.[21]

The precursor solution was delivered into the chip using a syringe pump (Cole-Parmer, United Kingdom) located outside of the NMR spectrometer as illustrated in Fig. 2. Hydrogen gas (gas purity 99.995%) was delivered from a cyliner located outside of the spectrometer at a flow rate set to 20 mL min^{-1} controlled using a mass-flow controller at the end of the gas line. The gas line was equipped with a valve selecting a flow of either hydrogen in thermal equilibrium or parahydrogen. Parahydrogen gas was obtained with 50% enrichment using a home-built parahydrogen generator filled with iron (III) oxide and cooled to 77 K.

All chemicals were purchased from Merck KGaA (Germany) and were used as received.

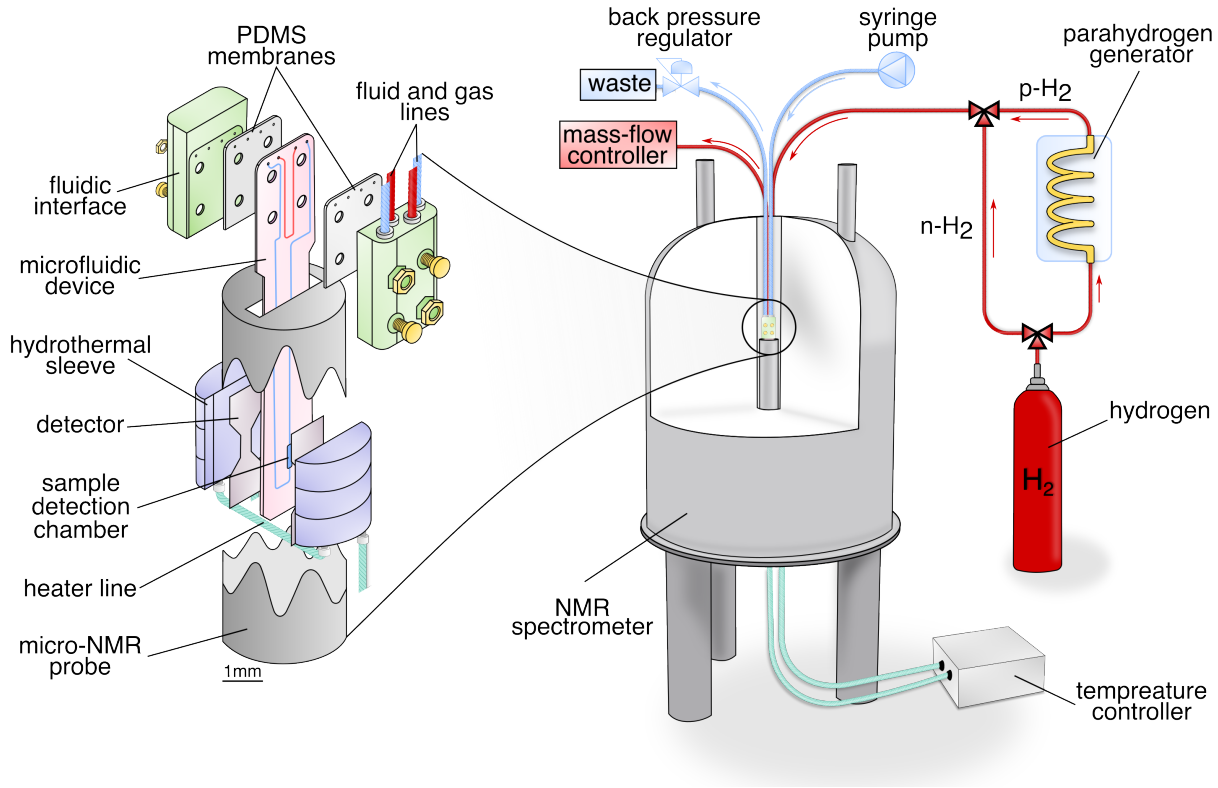

Figure 2: Experimental set up. Microfluidic chip assembly consisted of a microfluidic device interposed between two PDMS membranes, which were held together by the fluidic interface that enabled delivery of substrates into the chip. All experiments were performed inside of a high-field NMR spectrometer. Hydrogen/parahydrogen gas was supplied from a gas cylinder, while the precursor solution was introduced into the device using a syringe pump located outside of the spectrometer. The device was placed into the micro-NMR probe for detection. The probe was also equipped with hydrothermal sleeves regulated by temperature controller that enabled efficient heating of the sample detection chamber.

Quantification of Hydrogen Uptake into $\beta-$chip

The uptake of hydrogen into the $\beta-$chip was quantified by flowing a solution of 20 mM sodium acetate dissolved in methanol-d4. In the gas channel, hydrogen in thermal equilibrium was supplied at 5 bar. The flow rate of hydrogen was controlled using a flow meter positioned at the end of the gas line, set to a constant rate of 20 mL/min. The flow rate of the liquid was varied from 2 to 20 μL min^{-1} in steps of 2 μL min^{-1} and the solution was left to equilibrate for 10 minutes at each flow rate. Then, 64 scans were acquired after the application of a $\frac{\pi}{2}$ pulse with a recycle delay of 20 s.

Finite Element Modelling

Finite element simulations were performed using COMSOL Multiphysics version 5.4. Fig. 3a shows the simulation domain. The key functional components are: the fluid channel (56.6 mm length, 0.1 mm width), the sample chamber (2 mm length, 1 mm width) and two PDMS membranes (31.6 mm length, 0.4 mm width). The total volume of the β – chip was calculated as 7 μL. A detailed description of simulations in found in the SI.

Charcterization of Hyperpolarized Allyl Acetate Formation Kinetics

The precursor solution contained 5 mM of [1,4-bis(diphenylphospino)butane](1,5-cycloctadiene) rhodium (I) tetrafluoroborate and 20 mM of propargyl acetate dissolved in methanol-d4. Parahydrogen gas pressure was set to 5 bar. The nutation frequency for RF pulses was 125 kHz for protons. Spectra were collected with a 16 ppm spectral width and 8 k data points. Data was acquired continuously while varying the flow rate from 2 to 12 μL min^{-1} in steps of 1 μL min^{-1} and from 14 to 20 μL min^{-1} in steps of 2 μL min^{-1}. At each flow rate, 20 single scan spectra were acquired after the application of a $\frac{\pi}{4}$ pulse with a recycle delay of 30 s. At these experimental conditions, it took $\sim$ 2 minutes for the hyperpolarized signal to reach the sample chamber and stabilise therefore the first 10 transients at each flow rate were discarded to ensure that only steady-state data was taken into consideration as shown in Fig. 4.

Spectral integrals were derived by fitting two Lorentzian functions to the H^h signal, detailed fitting is shown in the SI. Reference spectra were obtained using hydrogen in thermal equilibrium instead of parahydrogen. 10 mM of isopropanol (IPA) was added as the concentration standard while other conditions remained identical. Addition a minimal amount of another solvent is not expected to negatively impact the reaction.

To obtain reference spectra, the solution was flowed at 5, 7 and 9 μL min^{-1} for 25 ± 3°C, 37 ± 3°C, and 47 ± 3°C, respectively. The pressure of hydrogen in thermal equilibrium was set to 5 bar, all other conditions remained identical. Each reference spectrum is an average of 512 transients with a 30 s recycle delay. The yield of allyl acetate was found by comparing the integral

of signal H^f peak at 5.9 ppm to the intensity of the isopropanol peak at 1.1 ppm and accounting for the difference in the number of protons. The yield of propyl acetate was calculated as described above, from the integral of H^i peak at 4.33 ppm to the intensity of the isopropanol peak. The enhancement factor was obtained by calculating the SNR in the thermal and reference spectra and accounting for the difference in the number of scans.

Formation of ^{13}C Hyperpolarized Fumarate

The precursor solution contained 100 mM acetylene dicarboxylic acid [1-^{13}C] disodium salt, 6 mM $[RuCp^*(CH_3CN)_3]PF_6$ catalyst and 200 mM sodium sulfite dissolved in D_2O at 50°C. The heater temperature was set to 58°C. Flow rates from 2 to 18 $\mu L\,min^{-1}$ in steps of 2 $\mu L\,min^{-1}$ were studied. Parahydrogen pressure was set to 6 bar. The probe delivered nutation frequencies for ^{13}C RF pulses of 12.5 kHz. Spectra were collected with a 200 ppm spectral width, and 8 k data points were acquired. Proton singlet order in [1-^{13}C]fumarate was converted into the observable carbon magnetisation using the singlet-to-heteronuclear-magnetisation (S2hM) pulse sequence.[35] The maximum efficiency was achieved using the following parameters: $\tau = 15.7$ ms, $n_2 = 7$, $n_1 = 7$. The repetition delay was set to 60 s. To calculate the enhancement factor for carbon polarization, the SNR of in the hyperpolarized spectrum was compared with the SNR obtained form a spectrum of 1M D-glucose-1-^{13}C averaged over 32 scans.

Results and Discussion

Enhancing Hydrogen Uptake into $\beta-$chip

An insufficient uptake of hydrogen into the $\alpha-$chip proposed by Eills *et al.*[27] was identified as the main cause of the low yield of the PHIP reaction shown in Fig. 1a.[28] Simply elevating hydrogen pressure to increase the partial pressure of hydrogen in the chip is not a viable solution due to engineering challenges such chip delamination, which leads to leakages. Moreover, working with

high hydrogen pressures poses an increased safety hazard. Instead, the channel network can be modified to maximise the gas uptake. The fluidic design in the $\alpha-$chip used by Ellis *et al.* consisted of one gas and one fluid channel in a side-by-side arrangement, with a PDMS membrane covering both channels and serving as a diffusion conduit for H_2. The fluid channel in the $\beta-$chip design was positioned between two gas pathways, as shown in Fig. 3a and b. This arrangement effectively doubles the area of the fluid channel that comes into contact with the PDMS membrane. Additionally, the fluid pathway was extended by 30%.

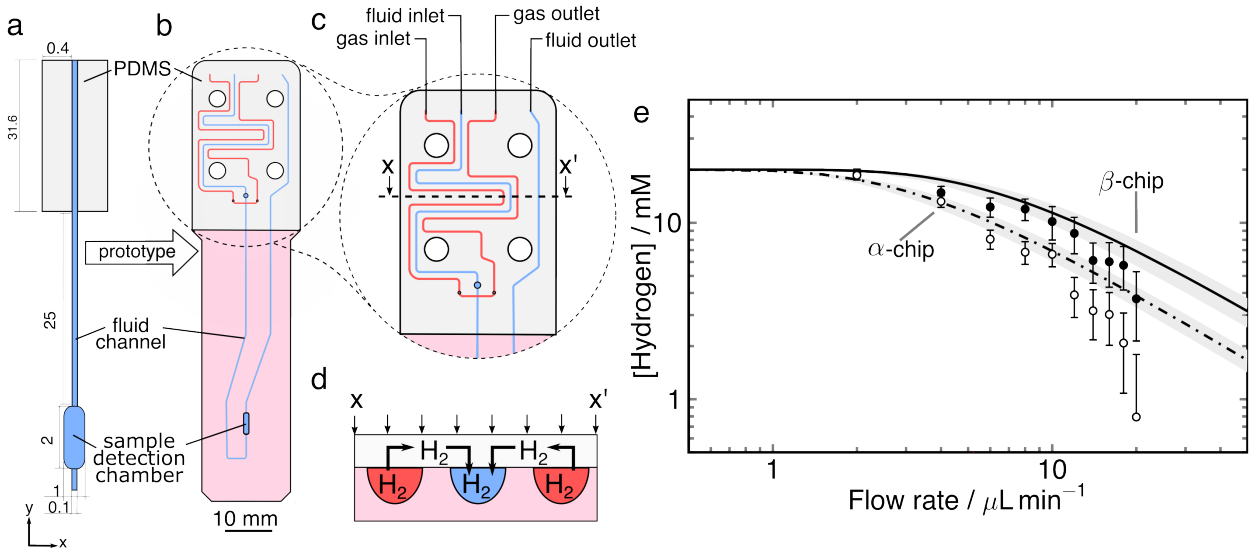

Figure 3: a) The simulation domain used in the finite element modelling of the $\beta-$chip. b) The top view of the $\beta-$chip where the fluid channel was interposed between two gas channels in order to increase the uptake of hydrogen into the chip. c) The key area of the chip enlarged. d) The cross section of the chip illustrating hydrogen diffusion of from the gas channel (red) to the solution channel (blue) e) Hydrogen uptake into the chip as a function flow rate. The black circles represent NMR data and the error bars were calculated form the SNR variation. The black solid line is the result of an FEM simulation. The grey shadow is the $\pm 1.5\,\mu$L error in the volume of the chip.

To measure the uptake of hydrogen gas into the $\beta-$chip, methanol was flowed into the fluid channel by means of a syringe pump located outside of the NMR spectrometer as shown in Fig. 2. The chip was pressurised to 5 bar with hydrogen gas and its flow was controlled using a mass-flow controller set to 20 mL min^{-1}. Dissolved hydrogen was detected by NMR in the 2.5 μL sample chamber on the chip.

Fig. 3e shows the concentration of hydrogen in the sample chamber as a function of flow rate;

20 mM of sodium acetate was used as the concentration standard. The solid empty and black circles represent the NMR data for $\alpha-$ and $\beta-$chips, respectively. Error bars were calculated from the SNR variation. Data for the $\alpha-$chip was obtained from Ref.[27] At 2 μL min^{-1} flow rate the flowing liquid in both devices is fully saturated with hydrogen. However, as the flow rate increases to 10 μL min^{-1}, the concentration of hydrogen in the $\beta-$chip is 11.3 mM versus only $\sim$6 mM in the $\alpha-$chip. At a higher flow rate of 18 μL min^{-1} there is 3 times more hydrogen dissolved in the $\beta-$chip compared to the $\alpha-$chip. The solid and dash-dotted lines are the FEM simulations and the gray shadows represent a $\pm$1.5 μL error in the volume of the chips. The error in volume likely comes from imperfection in the bonding procedure and from imprecise cutting of the microstructures within the chip. To obtain precise volume of the chip one could obtain CT images however, each chip would have to be imaged. This is due to the manual fabrication of our devices, resulting in inherent variability within each unit. However, implementing such solutions would be costly.

Simulations for both $\alpha-$ and $\beta-$chip are in good agreement with the experimental data for flow rates up to 10 μL min^{-1}. Above this flow rate, the behaviour is not predicted well. This discrepancy is not well understood yet, it was proposed that this could be due to the deformation of the PDMS membrane.[27]

Temperature Dependence of Hyperpolarized Allyl Acetate Formation

The PHIP reaction was performed by flowing the precursor solution containing 20 mM of propargyl acetate **PR** and 5 mM of rhodium catalyst into the solution channel and delivering 5 bar of *para*-enriched hydrogen gas into the gas channel. Fig. 4a shows a single scan proton NMR spectrum acquired after a $\frac{\pi}{4}$ pulse. The spectra were acquired during a steady-state experiment, with the solution continuously flowed at a rate of 5 μL min^{-1}. The hyperpolarized spectrum contains an antiphase doublet at 5.2 ppm corresponding to protons H^h and an antiphase multiplet at 5.9 ppm corresponding to protons H^f. This is compared with a 512-scans reference spectrum obtained with hydrogen in thermal equilibrium shown in Fig. 4b. Each scan was acquired after a $\frac{\pi}{2}$ pulse with

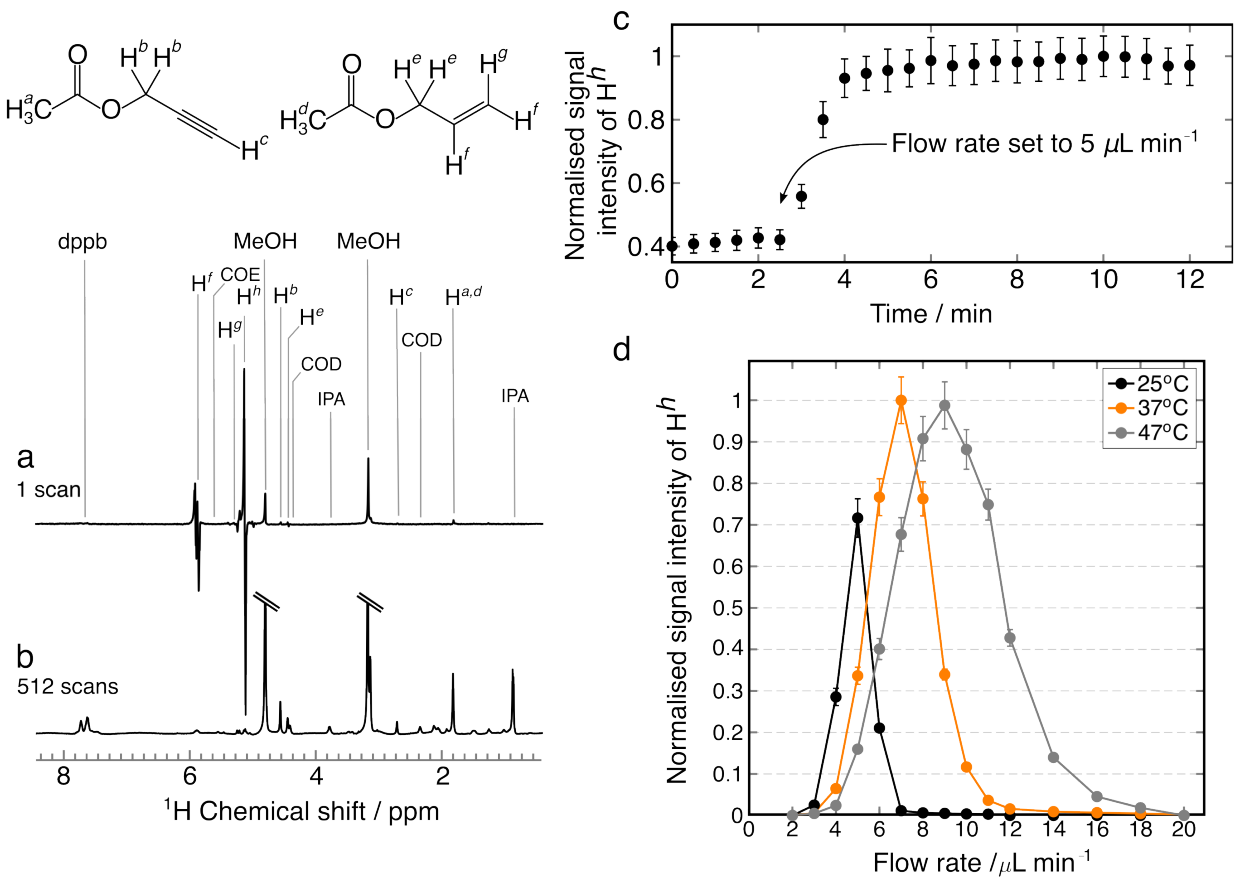

Figure 4: a) Single-scan proton spectrum obtained with *para*-hydrogen. b) Reference spectrum obtained with hydrogen in thermal equilibrium. Methanol peaks have been suppressed for clarity. c) Build-up of hyperpolarized signal (H^h) after changing the flow rate from 4 to 5 μL min^{-1}. d) Flow-rate dependence of the hyperpolarized allyl acetate yield at three different temperatures. Black, orange and orange dots represent the experimental data for data obtained at room temperature 25 ± 3°C, 37 ± 3°C and 47 ± 3°C respectively. Solid lines have been included as guides to the eye.

a recycle delay of 30 s. From the ratio of the signal intensity in the reference and hyperpolarized spectra, the ^{1}H polarization was estimated. In the reference spectrum, the SNR was found to be 9:1, while it was 300:1 in the hyperpolarized spectrum. Since the reference spectrum was obtained using 512 scans, the SNR resulting from a single scan would be $9/\sqrt{512} \approx 0.40$. Therefore, the signal enhancement factor is $\varepsilon \approx 300/0.4 \approx 750$. At the field of 11.7 T and temperature of 25 ± 3°C this corresponds to 3% ^{1}H polarization.

At 5 μL min^{-1} flow rare, the concentration of propargyl acetate was 4.9 ± 0.2 mM, which corresponds to 24.5 ± 0.25% yield. This was calculated by comparing the intensity of the isopropanol peak at 1.14 ppm in the reference spectrum to the intensity of the H^f peak and accounting for the difference in the number of protons. By introducing an additional gas channel the yield of allyl acetate was increased over 15-fold compared with the α – chip.[27]

Fig. 4c shows the buildup of a hyperpolarized signal H^h after changing the flow rate from 4 to 5 μL min^{-1}. NMR spectra were acquired every 30 s using a $\frac{\pi}{4}$ excitation pulse. The signal intensity begins to rise 30 s after the target flow rate was set to 5 μL min^{-1} and it reaches a steady-state after 2 minutes. Similar results were shown in Ref[27] where the signal intensity also took just 2 minutes to build-up. After reaching a steady-state the system provides a remarkable stability of the signal.

Accurate temperature regulation is a crucial aspect of biological and chemical platforms. In this study, we've implemented variable temperature control by inserting hydrothermal sleeves between the stripline detector, housing the microfluidic device, effectively heating the sample detection chamber. Overall, the sample chamber of the chip is efficiently heated to a desired temperature with a temperature variation of $\pm$ 3°C from the target temperature, which sufficient for this application.[21]

Fig. 4d shows the normalised signal intensity of proton (H^h) as a function of flow rate at three temperatures. The black, orange and gray solid circles correspond to experimental data obtained at 25 ± 3°C, 37 ± 3°C and 47 ± 3°C respectively. Each data point on the graph is a mean of 10 integrals of peak H^h obtained from consecutive acquisitions. As the temperature is increased form 25 ± 3 to 37 ± 3°C, the maximum of the signal increases by 30%. Upon further 10°C temperature

increase, the maximum signal decreases by 2%. Increasing the temperature by 10°C shifts the position of the maximum by +2°C μL min^{-1}. At 25 ± 3°C the maximum is located at 5 μL min^{-1}, while at 47 ± 3°C it is at 9 μL min^{-1}. The position of the maximum represents a balance between the rate of relaxation of the hyperpolarized product and the hydrogen uptake into the chip. At low flow rates such as 2 μL min^{-1}, the residence time of the hyperpolarized product in the fluid channel is very long therefore it fully relaxes before it reaches the sample chamber. As the flow rate increases, the product is delivered faster to the sample chamber and less of it is lost due to relaxation hence the steep spike from 2 μL min^{-1}till the maximum. As the temperature increases so do the reaction rates hence the position of the maximum shifts to a higher flow rate as the product needs to be delivered faster into the sample chamber.

In order to determine the yield of allyl acetate at the optimum flow rate, the experiment was repeated using hydrogen in thermal equilibrium. 10 mM isopropanol was used as the concentration standard and the thermal spectra are shown in the SI. The results are listed in Table 1.

The concentration of allyl acetate at 25 ± 3 °C was found to be 4.9 ± 0.2 mM, which corresponds to 24.5 ± 1% yield. The same calculations were repeated for data obtained at 37 ± 3°C and 47 ± 3°C. The concentration of allyl acetate at the optimal flow at 37 ± 3°C was found to be 7.0 ± 0.2 mM, resulting in the yield of 35.0 ± 1.0%. This is a further increase of 10% in the yield. Increasing the temperature further to 47 ± 3°C, resulted in a drop in the concentration of **AL** to 5.4 ± 0.2 mM. At 37 ± 3°C the reaction is most efficient and even leads to the formation of propyl acetate, as evidence by a H^i peak at 4.33 ppm in Fig. 1, which is absent at other temperatures. The concentration of propyl acetate was calculated as 1.2 ± 0.2 mM.

From the ratio of the signal intensity in the reference and hyperpolarized spectra, the ^{1}H polar-

Table 1: Experimental results for the PHIP reaction in the β − chip performed at 25 ± 3°C, 37 ± 3°C and 47 ± 3°C.

T / °C	**q / μL min^{-1}**	**[AL] / mM**	ε	**^{1}H polarization / %**	**Molar polarization / μ M**
25	5	4.9 ± 0.2	750	3.0	147 ± 6
37	7	7.0 ± 0.2	1060	4.1	287 ± 8
47	9	5.2 ± 0.2	930	3.5	182 ± 7

ization was estimated. Accounting for the difference in the number of scans, the signal enhancement was calculated as 750. At the field of 11.7 T and temperature of 25 ± 3°C, this corresponds to 3.0% ^{1}H polarization. The enhancement factor for reactions conducted at 37 ± 3°C and 47 ± 3°C was found to be 1060 and 930, indicating proton polarizations of 4.1% and 3.5%, respectively. The polarization level for the $\alpha-$chip was reported as 8%,[27] which is a much higher polarization than obtained in the $\beta-$chip. However, for *in situ* studies spin polarization may not be a sufficient measure as the total number of spins detected also depends on the molar concentration of the species. Instead, molar polarization should be considered, which is defined as the product of the polarization level and the concentration of the species.[36] Molar polarization for the $\beta-$chip was calculated as 147 ± 6, 287 ± 8, 182 ± 7 μM, for reactions preformed at 25 ± 3°C, 37 ± 3°C, and 47 ± 3°C, respectively, while the molar polarization for the $\alpha-$chip was less than 40 μM. By implementing an additional hydrogenation pathway in the $\beta-$chip the molar polarization has nearly quadrupled compared with the $\alpha-$chip. Elevating temperature of the reaction by 10°C further approximately doubled the molar polarization. However at 47°C, molar polarization decreased.

Formation of ^{13}C Hyperpolarized Fumarate

The short lifetime of ^{1}H polarization, which is of the order of seconds, limits application of proton-hyperpolarization *in vivo* as longer observation times are required. This can be overcome by transferring the polarization to a longer-lived nucleus such as carbon-13 or nitrogen-15. Hyperpolarized fumarate is a promising target for *in vivo* detection of necrosis and therefore has been extensively used as a hyperpolarization target.[36–39] However, the trans-hydrogenation reaction to synthesise hyperpolarized fumarate is challenging as it is slow compared to the timeframe in which the hyperpolarization returns to thermal equilibrium.[40] The advancements detailed in this paper improve reaction conditions by enabling the elevation of reaction temperatures and enhancing hydrogen concentration within the device hence make it possible to hyperpolarize fumarate more efficiently.

As shown in Fig. 5a hyperpolarized fumarate was generated via a reaction of [1$-^{13}$C]-acetylene-dicarboxylic acid disodium salt (**ADCA**) with *para*−hydrogen in a presence of a ruthenium cata-

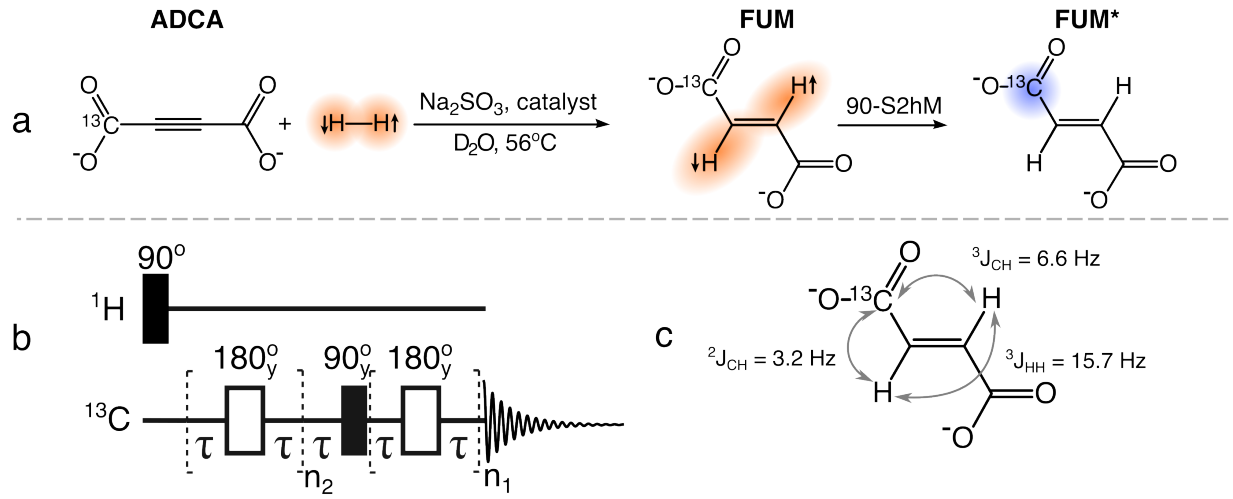

Figure 5: a) Formation of ^{13}C hyperpolarized fumarate. acetylene dicarboxylic acid [1-^{13}C] disodium salt labelled as molecule **ADCA** reacts with parahydrogen in the presence of sodium sulfite and the catalyst $[RuCp^*(CH_3CN)_3]PF_6$ in D_2O. The reaction results in a production of disodium [1-^{13}C]fumarate, molecule **FUM**, with the two protons in a singlet state. Application of the S2hM pulse sequence converts the singlet state into a state that is magnetic and hence observable **FUM***. b) 90-S2hM pulse sequence used to transfer the polarization from the proton singlet state to carbon. The following parameters were found to be optimal for the sequence: $\tau = 15.8\,\mu s$, $n_1 = 7$, $n_2 = 7$. c) b) The $J-$coupling network of [1-^{13}C]fumarate. The $J-$coupling values were taken from Ref.[37]

lyst that resulted in a trans-hydrogenated product, a molecule of $[1-^{13}C]$fumarate(**FUM**). Since the added protons on the molecule of fumarate are chemically and magnetically equivalent, a ^{13}C label was introduced at one of the carboxylate groups to break their symmetry. This hydrogenation reaction is known to be affected by the singlet-triplet (S-T) mixing phenomenon, which can lead to a reduction of observable PHIP signal.[41] It occurs when molecules of hydrogen form intermediate hydride species with the catalyst metal center and at high field they experience a chemical shift difference. This can lead to a significant leakage from the proton singlet state ($|S_0\rangle$) to the central triplet state ($|T_0\rangle$).[42] There are methods for mitigating S-T mixing.[41,43,44] A $\pi/2$ "purge" pulse prior to the S2M sequence was found to improve the efficiency of the sequence in microfluidic chips.[33] The purge pulse removes the detrimental population of the $|T_0\rangle$ state by transferring it to the two outer $|T_\pm\rangle$ states where it has no effect on the polarization transfer. Here, the purge pulse was applied on the ^{1}H channel prior to application of the S2hM sequence on the ^{13}C channel as

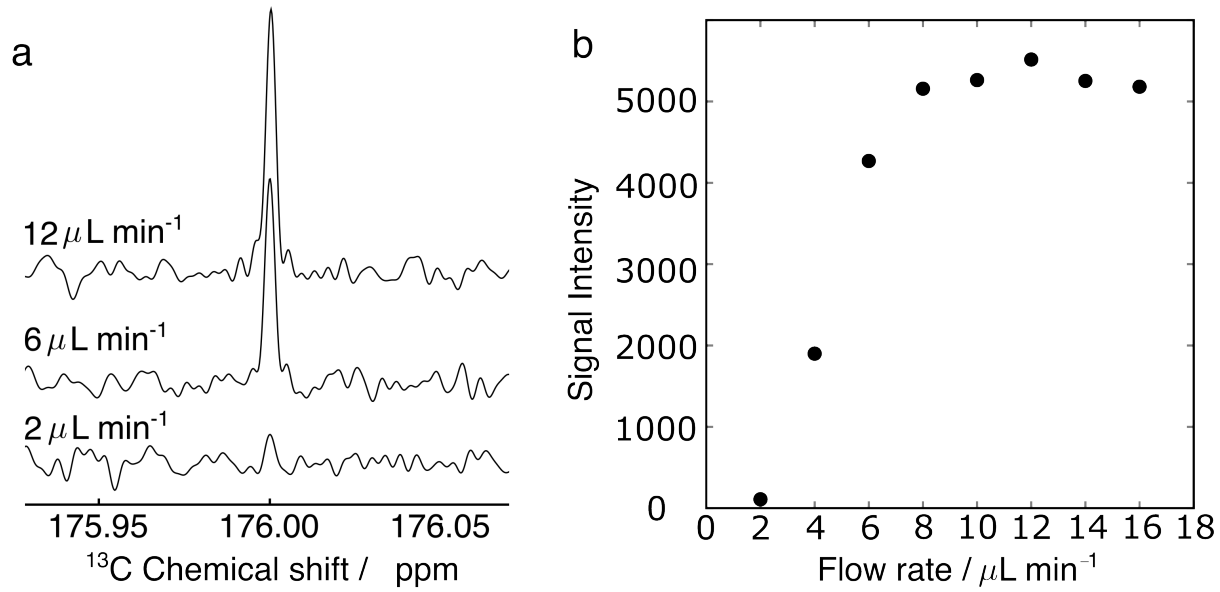

Figure 6: a) ^{13}C spectra of [1-^{13}C]fumarate at different flow rates. b) A plot of the signal intensity of [1-^{13}C]fumarate as a function of flow rate.

shown in Fig. 5c.

The set-up depicted in Fig. 2 and the $\beta-$chip was used to produce ^{13}C-hyperpolarized fumarate. Fig. 6a shows single scan carbon spectrum of ^{13}C-hyperpolarized fumarate at different flow rates. At 2 μL min^{-1}, the carbon signal is barely distinguishable from the noise but as the flow rate increases, the signal intensity increases. The change in signal intensity as a function of flow rate is displayed in Fig. 6b. Until 8 μL min^{-1}, there is a near-linear increase in the product formation then the signal intensity plateaus. This reaction profile is markedly different to the ones reported in the previous chapters. At very low flow rates, the time it takes for the product to be delivered into the sample chamber is greater that the relaxation time therefore, the product is formed upstream from the sample chamber and is passively carried into the detection chamber. As a result, increasing the flow rate results in a faster delivery of the product however since carbon nuclei relax at a much slower rate compared to proton nuclei the initial reaction profile is much smoother compared with the reaction profile discussed in the previous chapter. After 8 μL min^{-1} flow rate, the intensity of the signal $\sim$ plateaus. This is likely due to the fact that the reaction is slow and uptake of hydrogen into the chip is no longer limiting the rate of the reaction.

Detection of ^{13}C signals arising from thermally polarized fumarate was not possible using our home-built transmission line probe due to the limited sensitivity. To estimate the signal enhancement, the hyperpolarized spectrum was compared with a spectrum of 1M D-glucose-1-^{13}C obtained after the application of $\frac{\pi}{2}$ pulse; shown in the SI. The SNR in the glucose spectrum is 2:1, while in the hyperpolarized spectrum of fumarate the SNR is 9:1. Since glucose spectrum was obtained from 32 number of scans, the SNR in a single scan is $\frac{2}{\sqrt{32}} \approx 0.35$. Accounting for the fact that glucose spectrum was obtained from 1 M sample and spectrum of fumarate was obtained from 3 mM sample, this leads to the signal enhancement factor of $\varepsilon = \frac{9}{0.35} * \frac{1000}{3} \approx 8500$. Leading to 8.5% carbon polarization.

Conclusions

In this work we have used finite element simulations and modelling to aid design of an optimized microfluidic device for performing PHIP reactions. FEM of the chip reported by Ostrowska *et al.*[28] identified that inadequate uptake of hydrogen into the device is the limiting factor for the reaction, which resulted in sub-milimolar reaction yield.

Introduction of an additional hydrogenation channel resulted in at least 2-fold increase in hydrogen uptake into the device and consequently led to a 15-fold increased in the yield of hyperpolarized allyl acetate compared with previously reported α – chip.[27] Heating the sample chamber of the chip led to a further 10% increase in the yield.

Lastly, the same chip was used to transfer polarization to fumarate and obtain 8.5% carbon polarization.

While the reactions reported in this manuscript are not yet suitable for biological applications due to the presence of potentially toxic compounds for cell culture, they represent a crucial step towards the integrated production of hyperpolarized materials and cell culture. Devices based on similar designs have been successfully employed to quantify the metabolism of liver and breast cancer monolayers[21] and breast cancer spheroids,[20] underscoring the potential of this approach

for future biologically relevant applications.

Acknowledgments

Authors thank Dr. Manvendra Sharma for help with the hardware. This work was supported by the UK Engineering and Physical Sciences Research Council (EPSRC) through grants EP/W020343/1 and EP/V055593/1, and the iCASE studentship EP/R513325/1 to SJB, co-funded by Bruker UK Ltd. This research was also supported by the European Research Council grant 786707-FunMagResBeacons.

References

(1) Leung, C. M.; de Haan, P.; Ronaldson-Bouchard, K.; Kim, G.-A.; Ko, J.; Rho, H. S.; Chen, Z.; Habibovic, P.; Jeon, N. L.; Takayama, S.; Shuler, M. L.; Vunjak-Novakovic, G.; Frey, O.; Verpoorte, E.; Toh, Y.-C. A guide to the organ-on-a-chip. *Nat. Rev. Methods Primers* **2022**, *2*, 1–29.

(2) Ma, C.; Peng, Y.; Li, H.; Chen, W. Organ-on-a-Chip: A New Paradigm for Drug Development. *Trends Pharmacol. Sci.* **2021**, *42*, 119.

(3) Ingber, D. E. Human Organs-on-Chips for Disease Modelling, Drug Development and Personalized Medicine. *Nat. Rev. Genet.* **2022**, *23*, 467–491.

(4) Si, L.; Bai, H.; Rodas, M.; Cao, W.; Oh, C. Y.; Jiang, A.; Moller, R.; Hoagland, D.; Oishi, K.; Horiuchi, S.; Uhl, S.; Blanco-Melo, D.; Albrecht, R. A.; Liu, W.-C.; Jordan, T.; Nilsson-Payant, B. E.; Golynker, I.; Frere, J.; Logue, J.; Haupt, R.; McGrath, M.; Weston, S.; Zhang, T.; Plebani, R.; Soong, M.; Nurani, A.; Kim, S. M.; Zhu, D. Y.; Benam, K. H.; Goyal, G.; Gilpin, S. E.; Prantil-Baun, R.; Gygi, S. P.; Powers, R. K.; Carlson, K. E.; Frieman, M.; TenOever, B. R.; Ingber, D. E. A Human-Airway-on-a-Chip for the Rapid Identi-

fication of Candidate Antiviral Therapeutics and Prophylactics. *Nat. Biomed. Eng.* **2021**, *5*, 815–829.

(5) Wu, Q.; Liu, J.; Wang, X.; Feng, L.; Wu, J.; Zhu, X.; Wen, W.; Gong, X. Organ-on-a-chip: Recent Breakthroughs and Future Prospects. *Biomed. Eng. Online* **2020**, *19*, 1–19.

(6) Kolluri, N.; Klapperich, C. M.; Cabodi, M. Towards Lab-on-a-Chip Diagnostics for Malaria Elimination. *Lab Chip* **2017**, *18*, 75–94.

(7) Wu, J.; Dong, M.; Rigatto, C.; Liu, Y.; Lin, F. Lab-on-Chip Technology for Chronic Disease Diagnosis. *NPJ Digit. Med.* **2018**, *1*, 1–11.

(8) Jodat, Y. A.; Kang, M. G.; Kiaee, K.; Kim, G. J.; Martinez, A. F. H.; Rosenkranz, A.; Bae, H.; Shin, S. R. Human-Derived Organ-on-a-Chip for Personalized Drug Development. *Curr. Pharm. Des.* **2018**, *24*, 5471–5486.

(9) Cong, Y.; Han, X.; Wang, Y.; Chen, Z.; Lu, Y.; Liu, T.; Wu, Z.; Jin, Y.; Luo, Y.; Zhang, X. Drug Toxicity Evaluation Based on Organ-on-a-chip Technology: A Review. *Micromachines* **2020**, *11*, 381.

(10) Komen, J.; Westerbeek, E. Y.; Kolkman, R. W.; Roesthuis, J.; Lievens, C.; van den Berg, A.; van der Meer, A. D. Controlled Pharmacokinetic Anti-Cancer Drug Concentration Profiles Lead to Growth Inhibition of Colorectal Cancer Cells in a Microfluidic Device. *Lab Chip* **2020**, *20*, 3167–3178.

(11) Emami Nejad, A.; Najafgholian, S.; Rostami, A.; Sistani, A.; Shojaeifar, S.; Esparvarinha, M.; Nedaeinia, R.; Haghjooy Javanmard, S.; Taherian, M.; Ahmadlou, M.; Salehi, R.; Sadeghi, B.; Manian, M. The Role of Hypoxia in the Tumor Microenvironment and Development of Cancer Stem Cell: A Novel Approach to Developing Treatment. *Cancer Cell Int.* **2021**, *21*, 1–26.

(12) Park, S.; Rintaro, H.; Kim, S. K.; Park, I. Characterization of Distinctive In Vivo Metabolism between Enhancing and Non-Enhancing Gliomas Using Hyperpolarized Carbon-13 MRI. *Metabolites* **2021**, *11*, 504.

(13) Park, I.; Kim, S.; Pucciarelli, D.; Song, J.; Choi, J. M.; Lee, K.-H.; Kim, Y. H.; Jung, S.; Yoon, W.; Nakamura, J. L. Differentiating Radiation Necrosis from Brain Tumor Using Hyperpolarized Carbon-13 MR Metabolic Imaging. *Mol. Imaging Biol.* **2021**, *23*, 417–426.

(14) Perkons, N. R.; Johnson, O.; Pilla, G.; Profka, E.; Mercadante, M.; Ackerman, D.; Gade, T. P. F. Functional Genetic Screening Enables Theranostic Molecular Imaging in Cancer. *Clin. Cancer Res.* **2020**, *26*, 4581–4589.

(15) Perkons, N. R.; Johnson, O.; Pilla, G.; Gade, T. P. F. Pharmacodynamics and Pharmacokinetics of Hyperpolarized [1−^{13}C]-Pyruvate in a Translational Oncologic Model. *NMR Biomed.* **2021**, *34*, e4502.

(16) Martinho, R. P.; Bao, Q.; Markovic, S.; Preise, D.; Sasson, K.; Agemy, L.; Scherz, A.; Frydman, L. Identification of Variable stages in Murine Pancreatic Tumors by a Multiparametric Approach Employing Hyperpolarized ^{13}C MRSI, ^{1}H Diffusivity and ^{1}H T_1 MRI. *NMR Biomed.* **2021**, *34*, e4446.

(17) Woitek, R.; McLean, M. A.; Gill, A. B.; Grist, J. T.; Provenzano, E.; Patterson, A. J.; Ursprung, S.; Torheim, T.; Zaccagna, F.; Locke, M.; Laurent, M.-C.; Hilborne, S.; Frary, A.; Beer, L.; Rundo, L.; Patterson, I.; Slough, R.; Kane, J.; Biggs, H.; Harrison, E.; Lanz, T.; Basu, B.; Baird, R.; Sala, E.; Graves, M. J.; Gilbert, F. J.; Abraham, J. E.; Caldas, C.; Brindle, K. M.; Gallagher, F. A. Hyperpolarized ^{13}C MRI of Tumor Metabolism Demonstrates Early Metabolic Response to Neoadjuvant Chemotherapy in Breast Cancer. *Radiol. Imaging Cancer* **2020**, *2*, e200017.

(18) Woitek, R.; McLean, M. A.; Ursprung, S.; Rueda, O. M.; Garcia, R. M.; Locke, M. J.; Beer, L.; Baxter, G.; Rundo, L.; Provenzano, E.; Kaggie, J.; Patterson, A.; Frary, A.; Field-

Rayner, J.; Papalouka, V.; Kane, J.; Benjamin, A. J. V.; Gill, A. B.; Priest, A. N.; Lewis, D. Y.; Russell, R.; Grimmer, A.; White, B.; Latimer-Bowman, B.; Patterson, I.; Schiller, A.; Carmo, B.; Slough, R.; Lanz, T.; Wason, J.; Schulte, R. F.; Chin, S.-F.; Graves, M. J.; Gilbert, F. J.; Abraham, J. E.; Caldas, C.; Brindle, K. M.; Sala, E.; Gallagher, F. A. Hyperpolarized Carbon-13 MRI for Early Response Assessment of Neoadjuvant Chemotherapy in Breast Cancer Patients. *Cancer Res.* **2021**, *81*, 6004–6017.

(19) Badilita, V.; Meier, R. Ch.; Spengler, N.; Wallrabe, U.; Utz, M.; Korvink, J. G. Microscale Nuclear Magnetic Resonance: A Tool for Soft Matter Research. *Soft Matter* **2012**, *8*, 10583–10597.

(20) Patra, B.; Sharma, M.; Hale, W.; Utz, M. Time-Resolved Non-Invasive Metabolomic Monitoring of a Single Cancer Spheroid by Microfluidic NMR. *Sci. Rep.* **2021**, *11*, 53.

(21) Rogers, G.; Barker, S.; Sharma, M.; Khakoo, S.; Utz, M. Operando NMR Metabolomics of a Microfluidic Cell Culture. *J. Magn. Reson.* **2023**, *349:107405.*

(22) Jenne, A.; von der Ecken, S.; Moxley-Paquette, V.; Soong, R.; Swyer, I.; Bastawrous, M.; Busse, F.; Bermel, W.; Schmidig, D.; Kuehn, T.; Kuemmerle, R.; Al Adwan-Stojilkovic, D.; Graf, S.; Frei, T.; Monette, M.; Wheeler, A. R.; Simpson, A. J. Integrated Digital Microfluidics NMR Spectroscopy: A Key Step toward Automated In Vivo Metabolomics. *Anal. Chem.* **2023**, *95*, 5858–5866.

(23) Chen, J.; Tian, J.; Chen, Y.; Wu, T.; Sun, H.; Xie, J.; You, X.; Chen, Z. Probing the Kinetics of Chemical Reactions in Ultra-Small Droplet Samples Using Digital Microfluidic Nuclear Magnetic Resonance Spectroscopy. *Microchem. J.* **2023**, *193*, 108984.

(24) Bowers, C. R.; Weitekamp, D. P. Parahydrogen and Synthesis Allow Dramatically Enhanced Nuclear Alignment. *J. Am. Chem. Soc.* **1987**, *109*, 5541–5542.

(25) Duckett, S. B.; Sleigh, C. J. Applications of the Parahydrogen Phenomenon: A Chemical Perspective. *Prog. Nucl. Magn. Reson. Spectrosc.* **1999**, *34*, 71–92.

(26) Reineri, F.; Cavallari, E.; Carrera, C.; Aime, S. Hydrogenative-PHIP Polarized Metabolites for Biological Studies. *MAGMA* **2021**, *34*, 25–47.

(27) Eills, J.; Hale, W.; Sharma, M.; Rossetto, M.; Levitt, M. H.; Utz, M. High-Resolution Nuclear Magnetic Resonance Spectroscopy with Picomole Sensitivity by Hyperpolarization on a Chip. *J. Am. Chem. Soc.* **2019**, *141*, 9955–9963.

(28) Ostrowska, S. J.; Rana, A.; Utz, M. Spatially Resolved Kinetic Model of Parahydrogen Induced Polarisation (PHIP) in a Microfluidic Chip. *ChemPhysChem* **2021**, *22*, 2004–2013.

(29) Stevanato, G.; Ding, Y.; Mamone, S.; Jagtap, A. P.; Korchak, S.; Glöggler, S. Real-Time Pyruvate Chemical Conversion Monitoring Enabled by PHIP. *J. Am. Chem. Soc.* **2023**, *145*, 5864.

(30) Carrera, C.; Cavallari, E.; Digilio, G.; Bondar, O.; Aime, S.; Reineri, F. ParaHydrogen Polarized Ethyl-[1-^{13}C]pyruvate in Water, a Key Substrate for Fostering the PHIP-SAH Approach to Metabolic Imaging. *ChemPhysChem* **2021**, *22*, 1042–1048.

(31) Reineri, F.; Boi, T.; Aime, S. ParaHydrogen Induced Polarization of ^{13}C Carboxylate Resonance in Acetate and Pyruvate. *Nat. Commun.* **2015**, *6*, 1–6.

(32) Cavallari, E.; Carrera, C.; Aime, S.; Reineri, F. Studies to Enhance the Hyperpolarization Level in PHIP-SAH-produced C13-Pyruvate. *J. Magn. Reson.* **2018**, *289*, 12–17.

(33) Barker, S. J.; Dagys, L.; Hale, W.; Ripka, B.; Eills, J.; Sharma, M.; Levitt, M. H.; Utz, M. Direct Production of a Hyperpolarized Metabolite on a Microfluidic Chip. *Anal. Chem.* **2022**, *94*, 3260–3267.

(34) Sharma, M.; Utz, M. Modular Transmission Line Probes for Microfluidic Nuclear Magnetic Resonance Spectroscopy and Imaging. *J. Magn. Reson.* **2019**, *303*, 75–81.

(35) Stevanato, G.; Eills, J.; Bengs, C.; Pileio, G. A Pulse Sequence for Singlet to Heteronuclear Magnetization Transfer: S2hM. *J. Magn. Reson.* **2017**, *277*, 169–178.

(36) Knecht, S.; Blanchard, J. W.; Barskiy, D.; Cavallari, E.; Dagys, L.; Van Dyke, E.; Tsukanov, M.; Bliemel, B.; Münnemann, K.; Aime, S.; Reineri, F.; Levitt, M. H.; Buntkowsky, G.; Pines, A.; Blümler, P.; Budker, D.; Eills, J. Rapid Hyperpolarization and Purification of the Metabolite fumarate in Aqueous Solution. *Proc. Natl. Acad. Sci. U.S.A.* **2021**, *118*, e2025383118.

(37) Ripka, B.; Eills, J.; Kouřilová, H.; Leutzsch, M.; Levitt, M. H.; Münnemann, K. Hyperpolarized Fumarate *via* Parahydrogen. *Chem. Commun.* **2018**, *54*, 12246–12249.

(38) Stewart, N. J.; Nakano, H.; Sugai, S.; Tomohiro, M.; Kase, Y.; Uchio, Y.; Yamaguchi, T.; Matsuo, Y.; Naganuma, T.; Takeda, N.; Nishimura, I.; Hirata, H.; Hashimoto, T.; Matsumoto, S. Hyperpolarized ^{13}C Magnetic Resonance Imaging of Fumarate Metabolism by Parahydrogen-induced Polarization: A Proof-of-Concept *in vivo* Study. *ChemPhysChem* **2021**, *22*, 915–923.

(39) Eills, J.; Cavallari, E.; Carrera, C.; Budker, D.; Aime, S.; Reineri, F. Real-Time Nuclear Magnetic Resonance Detection of Fumarase Activity Using Parahydrogen-Hyperpolarized [1-^{13}CC]Fumarate. *J. Am. Chem. Soc.* **2019**, *141*, 20209–20214.

(40) Wienands, L.; Theiß, F.; Eills, J.; Rösler, L.; Knecht, S.; Buntkowsky, G. Optimizing the Reaction Conditions for the Formation of Fumarate via Trans-Hydrogenation. *Appl. Magn. Reson.* **2022**, *53*, 615–634.

(41) Kating, P.; Wandelt, A.; Selke, R.; Bargon, J. Nuclear Singlet/Triplet Mixing During Hydrogenations with Parahydrogen: an in situ NMR Method to Investigate Catalytic Reaction Mechanisms and Their Kinetics. 2. Homogeneous Hydrogenation of 1,4-dihydro-1,4-epoxynaphthalene Using Different Rhodium Catalysts. *J. Phys. Chem.* **1993**, *97*, 13313–13317.

(42) Markelov, D. A.; Kozinenko, V. P.; Knecht, S.; Kiryutin, A. S.; Yurkovskaya, A. V.;

Ivanov, K. L. Singlet to Triplet Conversion in Molecular Hydrogen and its Role in Parahydrogen Induced Polarization. *Phys. Chem. Chem. Phys.* **2021**, *23*, 20936–20944.

(43) Bargon, J.; Kandels, J.; Kating, P. Nuclear Magnetic Resonance Studies of Homogeneous Catalysis Using Parahydrogen: Analysis of Nuclear Singlet–Triplet Mixing as a Diagnostic Tool to Characterize Intermediates. *J. Chem. Phys.* **1993**, *98*, 6150–6153.

(44) Dagys, L.; Bengs, C.; Levitt, M. H. Low-frequency Excitation of Singlet–Triplet Transitions. Application to Nuclear Hyperpolarization. *J. Chem. Phys.* **2021**, *155*, 154201.